Magnetic flux penetration in Nb superconducting films with lithographically defined micro-indentations

J. Brisbois,[1] O.-A. Adami,[1] J. Avila Osses,[1] M. Motta,[2] W. A. Ortiz,[2] N. D. Nguyen,[1] P. Vanderbemden,[3] B. Vanderheyden,[3] R. B. G. Kramer,[4] and A. V. Silhanek[1]

[1]*Département de Physique, Université de Liège, B-4000 Sart Tilman, Belgium*
[2]*Departamento de Física, Universidade Federal de São Carlos, 13565-905 São Carlos, SP, Brazil*
[3]*SUPRATECS and Department of Electrical Engineering and Computer Science, Université de Liège, B-4000 Sart Tilman, Belgium*
[4]*Institut Néel, CNRS, Université Joseph Fourier, BP 166, 38042 Grenoble Cedex 9, France*

(Dated: February 2, 2016)

We present a thorough investigation by magneto-optical imaging of the magnetic flux penetration in Nb thin films with lithographically defined border indentations. We demonstrate that discontinuity lines (d-lines), caused by the abrupt bending of current streamlines around the indentations, depart from the expected parabolic trend close to the defect and depend on the shape and size of the indentation as well as on the temperature. These findings are backed up and compared with theoretical results obtained by numerical simulations and analytical calculations highlighting the key role played by demagnetization effects and the creep exponent n. In addition, we show that the presence of nearby indentations and submicrometer random roughness of the sample border can severely modify the flux front topology and dynamics. Strikingly, in contrast to what has been repeatedly predicted in the literature, we do not observe that indentations act as nucleation spots for flux avalanches, but they instead help to release the flux pressure and avoid thermomagnetic instabilities.

PACS numbers:

I. INTRODUCTION

Many applications of modern superconducting devices are based on thin film structures, where the response of the system is dominated by the component of the magnetic field perpendicular to the film surface. If the magnetic field is applied after cooling to temperatures under T_c, the flux is forced to enter through the borders of the sample. For a sample with perfect boundaries, the flux penetration is typically dictated by the demagnetization effects. For example, in a square sample, magnetic field first penetrates through the central part of each side while it is delayed when approaching the diagonals.[1] In reality, unavoidable geometrical imperfections along the sample border can act as nucleation points for flux penetration and substantially change the flux front profile.[2]

The most commonly modelled border defect consists of a single semicircular indentation sitting along the perimeter of a large superconducting sample. The fact that the current streamlines running parallel to the sample border must abruptly circumvent the semicircular defect encountered in their path gives rise to so-called discontinuity lines (d-lines). Along these lines, the external magnetic field is efficiently screened by the sharp bending of the current,[3] leaving clear visible imprints in the flux profile as local minima in the magnetic flux landscape. An additional consequence of border defects is that flux penetrates deeper into the sample, by an amount Δ, as compared to the penetration without indentations.[4]

In the framework of the Bean critical state model applicable to bulk superconducting samples without demagnetization effects, a circular cavity of radius R, where the density of current $j = 0$, positioned close to the sample's edge should give rise to a parabolic d-line determined by the equation[3,5,6]

$$y(x) = \frac{x^2}{R} - R, \tag{1}$$

holding for $x \geq R$, with the origin of the reference system $(x, y) = (0, 0)$ located at the center of the circle. Therefore, from the curvature $d^2y/dx^2 = 2/R$ of the parabola extending into the sample to distances much larger than the characteristic length scale of the defect, it should be possible to deduce the size of such a micron-scale defect. If the defect has a triangular or a rectangular shape instead, the d-lines should still encode information about the shape and size of the defect but their form will not longer be exactly parabolic. In addition, within the Bean model,[5] the excess penetration distance is $\Delta = R$. Later theoretical investigations have anticipated that these predictions are expected to be modified (i) when dealing with thin films,[4] where non-local electrodynamic effects play a major role, (ii) when the critical current density j_c is field dependent,[7] and (iii) when taking into account vortex creep and current crowding effects.[4,8]

Type II superconductors are characterized by a highly non-linear electric field-current density constitutive relation $E(j) = E_c(j/j_c)^n$, where $n(T, B)$ is the creep exponent, for $j < j_c$ (creep regime), and $E \propto j$ for $j > j_c$ (flux flow regime). The Bean critical state model corresponds to the limiting case where $n \to \infty$. It has however been pointed out that already for $n > 3$, the current streamlines are close to those predicted by the Bean

model, thus making it difficult to experimentally reveal the influence of variations in n.[9] Numerical simulations for thin film geometry by Vestgården *et al.*,[4] including the creep effects mentioned above, gave rise to a series of interesting predictions. Namely, (1) in contrast to bulk superconductors, the excess penetration distance Δ can be significantly larger than the indentation radius R; (2) larger indentations produce larger Δ; (3) as the applied magnetic field increases, Δ exhibits a non-monotonous dependence reaching a maximum $\Delta_{\rm m}$ at an intermediate field $H_{\rm m}$; (4) as n increases, both $\Delta_{\rm m}$ and $H_{\rm m}$ increase; (5) the locally enhanced electric field and Joule heating near edge indentations should facilitate the nucleation of thermal instabilities; (6) flux avalanches are expected to be larger and occur more frequently at the indentations.

Earlier theoretical studies by Gurevich and Friesen[8,9] had already shown that a narrow slit of length R, interrupting the otherwise straight current path, significantly perturbs the current and electric field distributions at distances as large as $L_\parallel \sim R\sqrt{n}$ in the direction of the current flow and spans to distances $L_\perp \sim Rn$ through the current-carrying cross section. This prediction may suggest that the parabolic boundary delimiting these perturbations, $L_\perp \approx L_\parallel^2/R$, and reminiscent of the Bean d-lines, should be rather independent of the creep exponent n, a feature that has not been investigated experimentally so far.

It is worth mentioning here that the Bean model in its simplest form and its extensions to include a creep exponent ignore the Meissner phase, i.e. assume a first critical field $H_{\rm c1} = 0$. As was demonstrated recently,[10] this oversimplification of the model needs to be revised in order to explain the low magnetic field regime in samples with microstructured borders. In this low field limit, Clem and Berggren[11] have shown, within the London limit, that the conglomeration of current streamlines around obstacles (current crowding effect) plays a major role in the nucleation of vortices at microindentations. In particular, they demonstrated that a triangular notch produces a more important current crowding than a semicircular defect and therefore reduces the critical current needed to introduce vortices into the sample. This has been shown to be particularly relevant to explain the propagation of thermomagnetic instabilities in microstructured superconducting films.[12]

To the best of our knowledge, as of today, a direct experimental evidence scrutinizing the theoretical predictions of flux penetration in a superconductor with indentations is still lacking. The few existing experimental reports typically involve rather large ($R \gg \lambda$) and irregular (uncontrolled shape) indentations.[2,4,19,20] It is then the main objective of this work to present an exhaustive experimental investigation of the flux penetration in rectangular Nb thin films with micron-sized indentations, lithographically defined within a resolution of a few nm. We investigate the effect of shape, size, and periodicity of these artificial cavities through direct visualization of the magnetic flux landscape by magneto-optical imaging. We demonstrate that the parabolas are wider (i.e. smaller curvature) than predicted by the Bean model. Numerical simulations show that the presence of demagnetizing effects play a crucial role in the concavity of the parabola. We also show that the curvature of the d-lines emerging from the defect decreases as the temperature is increased. Moreover, in opposition to what has been repeatedly suggested based on the Bean model,[2–4,13] indentations do not seem to be distinguished places for the nucleation of flux jumps but rather the opposite, a place where flux avalanches will not take place. The extension of our results to samples with defects inside rather than at the border of the films is straightforward. Since unwanted fabrication defects are ubiquitous in superconducting materials, our results may not be only of academic interest but also important for technological developments.

II. EXPERIMENTAL DETAILS

The 100 nm-thick Nb films were prepared in a home-built electron beam UHV evaporator. The base pressure before evaporating the film was 2×10^{-10} Torr and reached 2.5×10^{-8} Torr during the evaporation. The film was evaporated at a rate of 0.1 nm/s on a silicon substrate which was at room temperature (28°C before and 45°C after the process). The structures were patterned using a Zeiss scanning electron microscope equipped with Raith patterning generator. The mask was a 270 nm-thick PMMA single layer resist (AR-P 679.04). After development of the resist, a 50 nm-thick aluminium mask was evaporated in a Plassys electron beam evaporator. After lift-off of the aluminium film the niobium film was dry etched by a reactive ion etch (2 min with SF6 gas). Finally the remaining Al on top of the Nb structures was removed with a basic solution (Megaposit MF 26A Developer).

The different sample layouts investigated in this work are summarized in Fig. 1. Several rectangular samples of 400 μm $\times$ 800 μm size evaporated on the same substrate were measured at the same time. Performing simultaneous measurements guarantees the same magnetic field H and temperature T for all samples, thus allowing a reliable comparison between them. The indentations were introduced along the longest sides of the rectangular films. Single indentations were located at the midpoint of the longest side. We fabricated three different motifs: triangular (T), semicircular (C), and rectangular slit (S), as shown in the optical images of Fig. 1. For the triangular defect, we prepared five different sizes R: 0.5, 2, 5, 8, and 10 μm. Moreover, for the 10 μm-size triangular indentation, we investigated five different separations between neighbouring defects: a single indentation, 100, 50, 10, and 0 μm separation. The tags referring to each individual case are listed in the table of Fig. 1. For the sake of completeness, we have also measured a plain rectangular film without artificial indentations. In addition

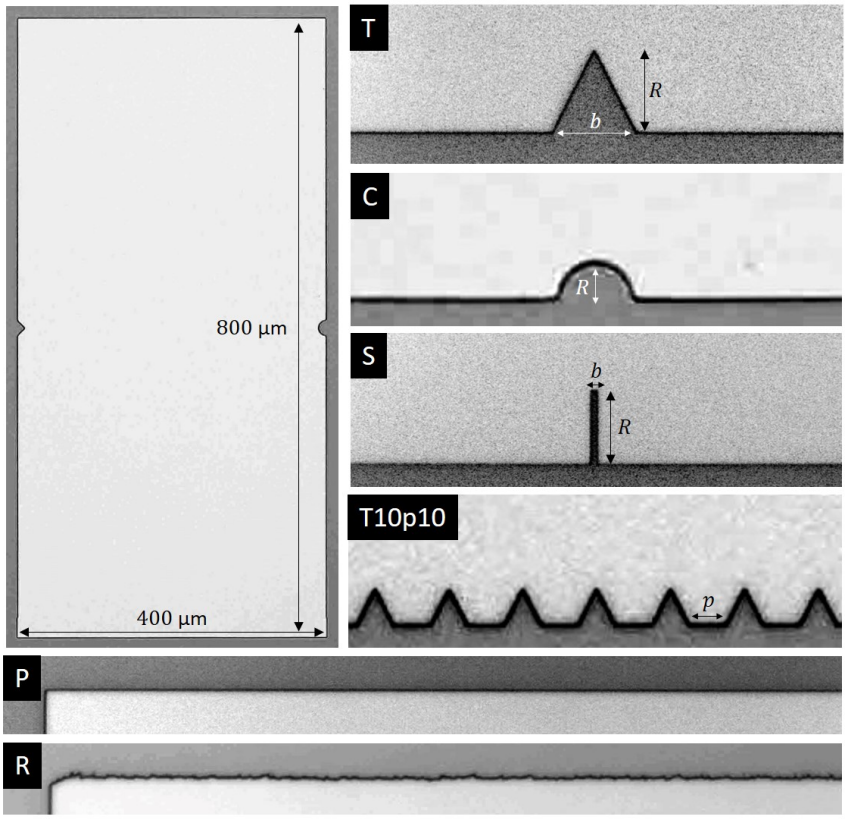

TAG	SHAPE	SIZE	PERIOD
T0.5		R = 0.5 µm b = 0.5 µm	∞
T2		R = 2 µm b = 2 µm	∞
T5		R = 5 µm b = 5 µm	∞
T8		R = 8 µm b = 8 µm	∞
T10		R = 10 µm b = 20 µm	∞
C		R = 10 µm	∞
S		R = 10 µm b = 1 µm	∞
P	plain film with smooth borders		
R	films with rough borders		
T10p0		R = 10 µm b = 10 µm	p = 0 µm
T10p10		R = 10 µm b = 10 µm	p = 10 µm
T10p50		R = 10 µm b = 10 µm	p = 50 µm
T10p100		R = 10 µm b = 10 µm	p = 100 µm

FIG. 1: In the upper left corner, an optical microscopy image shows the dimensions (400 μm × 800 μm) and the position of the artificial defects on the longest side for one of the Nb films. In this work, we studied 3 shapes of defects: triangular (T), semicircular (C) and rectangular (S). The corresponding panels show optical images of these indentations with the relevant distances reported in the table on the right side. The influence of the defect size and periodicity is studied for the triangular defect, where 5 sizes from 0.5 μm to 10 μm and 4 periods from 0 μm to 100 μm are considered (see panel T10p10 for an image for period 10 μm). For the sake of completeness, we also treat the case of a plain film with smooth borders (rugosity smaller than 0.2 μm) (P). Finally, we repeat the whole set of samples with rough borders of rugosity 0.8 μm (R).

to the previous samples, characterized by a roughness with a standard deviation of 0.03 μm, we have repeated the same set of 12 samples, but now with an artificial roughness[14] of 0.1 μm standard deviation along the long sides of the rectangular samples. This later case will allow us to comment about the robustness of our conclusions drawn from the ideal case.

The visualization of the magnetic flux landscape is performed through the Faraday rotation of 532 nm linearly polarized Hg light in a Bi-doped yttrium iron garnet with in-plane magnetic domains, a technique known as magneto-optical imaging.[6,15] This 3 μm-thick optical indicator has been epitaxially grown on a 450 μm-thick $Gd_3Ga_5O_{12}$ transparent substrate and has a Verdet constant of 2.9×10^5 rad $T^{-1}m^{-1}$. A 100 nm-thick Al mirror has been deposited on top of the indicator. The garnet is then placed on the sample, with the mirror side down. The sample is mounted on the cold-finger of a closed-cycle optical cryostat with temperature stability better than 0.01 K and base temperature of $\sim$ 4 K. The external magnetic field, in the range of $\pm$12 mT, is provided by a cylindrical copper coil fed by a Keithley-2440 current source. The whole setup is mounted on an actively damped optical table. All images were taken with a CCD camera RETIGA-4000 with 4.2 Mpixels of 7.4 μm × 7.4 μm pixel size, through an objective of 5× magnification, N.A.=0.13 and working distance 15 mm. Each pixel in the images corresponds to an area of $1.618 \times 1.618\,\mu m^2$. We have estimated a sensitivity of 5×10^{-2} mT^{-1} and an extinction coefficient of about 2×10^{-3} for our optical configuration. This value is indicative of the depolarisation of the light beam, occurring in the microscope, the cryostat windows and the garnet, and it is fair in comparison to other similar experimental setups.[16,17] In order to increase the signal-to-noise ratio, we recorded the average of 500 images. Post-image processing to remove fluctuations of intensity in the Hg-lamp, inhomogeneous illumination and field-independent background is done with specially tailored Matlab scripts and the ImageJ software. We took particular care to avoid the proliferation of magnetic domain walls in the indicator since in their presence, the local magnetic field is modified and the technique can therefore no longer be considered as non-invasive.[21]

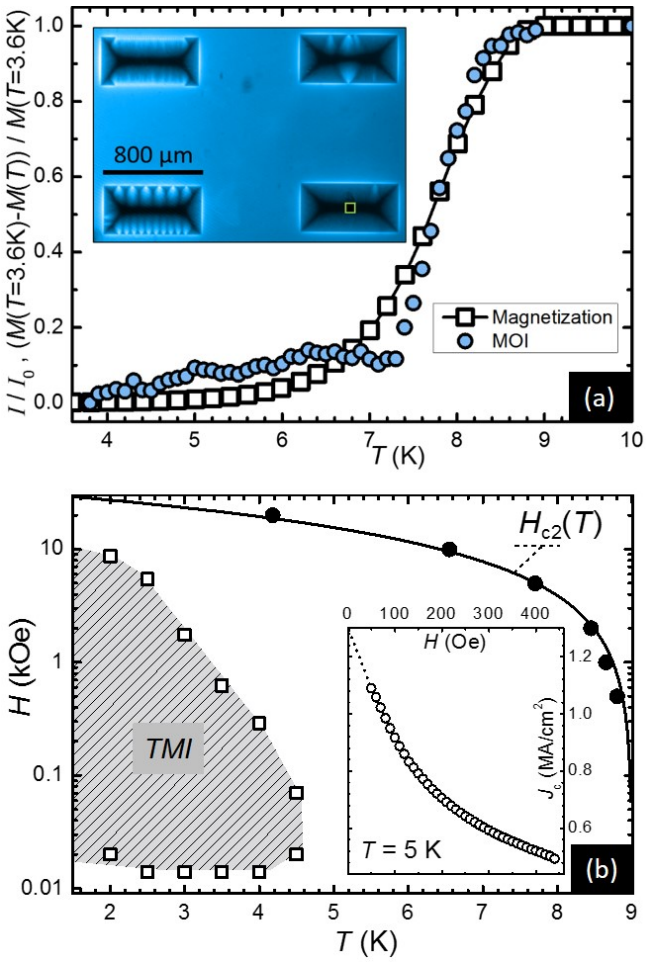

FIG. 2: (a) The critical temperature $T_c = 9$ K is determined by magnetization measurements (open squares). Similar measurements were carried with the magneto-optical imaging technique (MOI) by applying a field-cooling procedure with $\mu_0 H = 1$ mT and subsequently taking $\mu_0 H = 0$ mT (blue circles). Images of the samples are then taken for different temperatures and the average intensity I is measured in the 30×30 μm^2 square frame at the center of one sample (see inset). I is normalized by the intensity I_0 measured above T_c. The rectangular Nb samples shown in the inset have dimensions of $400 \times 800\,\mu$m^2. (b) Upper critical field $H_{c2}(T)$ obtained from magnetizations measurements in a 2×2 mm^2 Nb film without indentations. The line is a fitting based on the Ginzburg-Landau expression. The dashed area indicates the field-temperature region where thermomagnetic instabilities (TMI) develop. The inset shows the field dependence of the critical current density obtained from magnetization measurements at $T = 5$ K. The dotted line at low fields is a guide to the eye.

Fig. 2(a) shows the temperature dependence of the irreversible magnetization after zero-field cooling as measured by a SQUID magnetometer with $\mu_0 H = 1$ mT (square open symbols). The critical temperature $T_c = 9$ K is consistent with magneto-optical measurements obtained with the sample in the remanent state after field-cooling in $\mu_0 H = 1$ mT and subsequently setting $\mu_0 H = 0$ mT. As the temperature was increased, the average intensity (blue circles) was then tracked by the CCD camera in a square area of 30 μm $\times$ 30 μm in the center of one sample (square frame in the inset of Fig. 2(a)). The separation between neighbouring samples is 800 μm, thus ensuring negligible field cross talking between samples. The main panel of Fig. 2(b) shows the upper critical field $H_{c2}(T)$ as determined from $M(H)$ loops in a 2×2 mm^2 Nb film without indentations. By fitting these data with the Ginzburg-Landau expression $H_{c2}(T)=\Phi_0/2\pi\xi(T)^2$ where $\xi(T)=\xi(0)/\sqrt{1-T/T_c}$, we deduce $\xi(0)=9.7$ nm. The dashed area indicates the field-temperature region where thermomagnetic instabilities (TMI) develop as evidenced by sudden jumps in $M(H)$.[18] This region may slightly change from one experimental instrument to another, depending of the refrigeration power, environment, and heat removal efficiency. The inset shows the field dependence of the critical current density obtained from magnetization measurements at $T = 5$ K.

III. NUMERICAL MODELLING

The experimentally obtained isothermal magnetic flux penetration (i.e. in absence of thermomagnetic instabilities) will be compared with the macroscopic electromagnetic behavior of a superconductor characterized by a current dependent resistivity

$$\rho(j) = \rho_0 (j/j_c)^{n-1}, \tag{2}$$

where ρ_0 is the cut-off resistivity, j_c is the critical current density and n is the flux creep exponent. For the sake of completeness we treated two different cases. On the one hand, we modelled a superconducting system without non-local demagnetizing fields, the so-called longitudinal geometry. It is precisely within this configuration that Eq. (1) is valid. On the other hand, we modelled samples with strong demagnetizing fields, with the so-called transverse geometry, of particular importance when describing the field penetration in thin films such as in the present manuscript. In both cases, the resistivity in Eq. (2) was cut off to $\rho = \rho_0$ for $j > j_c$ in order for the simulations to converge; we checked that the resulting d-line are insensitive to the actual value used for the current cut-off. More details about each method are presented below.

A. Without demagnetization effects

For an infinitely long bar subject to a time-varying external homogeneous field $H_a(t)$ applied along the axis of the bar $\hat{\mathbf{z}}$, the total field $H(x,y,t) = H_a(t) + h(x,y,t)$, with $h(x,y,t)$ the current-induced field in the superconductor, becomes independent of z. It can be determined by Ref. 1:

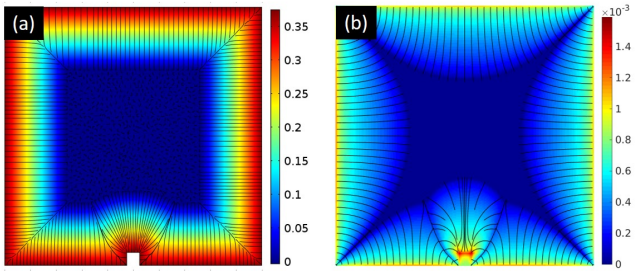

FIG. 3: Numerical simulations of the magnetic field h for similar partial flux penetration in a superconducting sample with a border defect (a) without and (b) with demagnetizing field. The streamlines converge to the d-lines. We used the parameters $\rho_0 = 10^{-14}\,\Omega$. m and $j_c = 10^{10}$ A.m^{-2}. In (b), the sample thickness is 100 nm.

$$\frac{\partial h}{\partial t} = \nabla \cdot (\rho \nabla h)/\mu_0 - \frac{\partial H_a}{\partial t}, \tag{3}$$

where $\rho(j)$ is given by Eq. (2), $\mathbf{j} = \nabla \times h\hat{\mathbf{z}}$, and $\mathbf{E} = \rho\,\mathbf{j}$. Equation (3) was integrated in a finite elements solver[22] with Dirichlet boundary conditions $h = 0$. The d-lines can be easily seen by plotting the streamlines of h, as shown in Fig. 3.

B. With demagnetization effects

As discussed by Brandt,[23] an accurate description of the currents and fields in a superconducting film must take into account the long range effects of the demagnetizing field. Following Ref. 23, the principal quantity to be calculated is the sheet current density

$$\mathbf{J}(x,y) = \int_{-d/2}^{d/2} dz \mathbf{j}(x,y,z), \tag{4}$$

where d is the film thickness. The sheet current can be derived from a stream function $g(x,y)$ that satisfies $\boldsymbol{J} = \nabla \times (\hat{\boldsymbol{z}} g) = (\partial g/\partial y, -\partial g/\partial x)$. By fixing $g = 0$ at the boundaries of the sample, it follows that $g(\boldsymbol{r})$ represents the total current passing between (x,y) and the border, in the case of a simply connected sample, and it is related to the perpendicular component of the magnetic field $H_z(x,y,0)$ by

$$H_z(\boldsymbol{r}) = H_a + \int_S d^2r' Q(\boldsymbol{r},\boldsymbol{r}') g(r'), \tag{5}$$

where H_a corresponds to an external field and the integral on the right stands for the demagnetizing field. S is the surface of the sample and the function $Q(\boldsymbol{r},\boldsymbol{r}')$ is the 2-dimension Biot-Savart kernel

$$Q(\boldsymbol{r},\boldsymbol{r}') = \lim_{z\to 0} \frac{2z^2 - |\boldsymbol{r}-\boldsymbol{r}'|^2}{4\pi(z^2+|\boldsymbol{r}-\boldsymbol{r}'|^2)^{5/2}}. \tag{6}$$

The constitutive relation $\boldsymbol{E} = \rho(J)\boldsymbol{J}/d$, along with the induction law $\mu_0 \boldsymbol{H} = -\nabla \times \boldsymbol{E}$, gives rise to the following expression for the total field:

$$\frac{\partial H_z}{\partial t} = \nabla \cdot (\rho \nabla g)/\mu_0 d. \tag{7}$$

Then, by taking the time derivative of Eq. (5), and inserting into Eq. (7), the following equation for g is obtained:

$$\int_S d^2r' Q(\boldsymbol{r},\boldsymbol{r}') \frac{\partial g(\boldsymbol{r}')}{\partial t} = \nabla \cdot (\rho \nabla g(\boldsymbol{r}))/\mu_0 d - \frac{\partial H_a}{\partial t}. \tag{8}$$

In this form, Eq. (8) cannot be easily time integrated.[23] In Fourier $\mathbf{k}$-space, by exploiting the fact that $\mathcal{F}(Q) \simeq k/2$,[24] and that the integral in Eq. (8) is a convolution, we obtain:

$$\frac{\partial g}{\partial t} = \mathcal{F}^{-1}\left(\frac{2}{k}\mathcal{F}\left(\nabla \cdot (\rho \nabla g)/\mu_0 d - \frac{\partial H_a}{\partial t}\right)\right), \tag{9}$$

with $k = |\boldsymbol{k}|$, and where $\mathcal{F}$ and $\mathcal{F}^{-1}$ denote the Fourier and inverse Fourier transforms respectively. The stream function can then be time integrated by Runge-Kutta. The calculation of $\partial g/\partial t$ however requires the determination of $\partial H_z/\partial t$ in the superconducting sample ($H_z^{\rm in}$) and in a small area outside the sample ($H_z^{\rm out}$) by an iterative method[24]

i) Initially, at $t = 0$, for the first iteration step $g = 0$, an approximation for $\partial g/\partial t$ is given by

$$\frac{\partial g_1}{\partial t} = \mathcal{F}^{-1}\left(\frac{2}{k}\mathcal{F}\left(-\frac{\partial H_a}{\partial t}\right)\right). \tag{10}$$

For later times, Eq. (9) should be used instead. The k^{-1} factor introduces a singularity when $k = 0$. This means that the zeroth order of the spectrum is undetermined and that $\partial g/\partial t$ can be shifted by an additive constant, chosen such that its average out of the sample is zero.

ii) Since g is known, the field inside the superconducting sample is calculated with Eq. (7). The field out of the sample is approximately obtained with

$$\frac{\partial H^{\rm out}_{z(i+1)}}{\partial t} = \frac{\partial H^{\rm out}_{z(i)}}{\partial t} - \mathcal{F}^{-1}\left(\frac{k}{2}\exp(-\delta^2 k)\mathcal{F}\left(\frac{\partial g_i^{\rm out}}{\partial t}\right)\right). \tag{11}$$

As steps i) and ii) are repeated, $\partial g_i^{\rm out}/\partial t$ goes to zero, and $\partial H^{\rm out}_{z(i)}/\partial t$ converges to its right value, except for an additive constant calculated by requiring that the area integral of $\partial H_{z(i)}/\partial t - \partial H_{a(i)}/\partial t$ is zero. The $\exp(-\delta^2 k)$ factor in Eq. (11) corresponds to a filter aimed to cut the high frequency components that are amplified by the $k/2$ term, and leads to divergence of the method. The parameter δ corresponds to the separation between grid points in real space.

The simulations have been performed for a Nb film with $\rho_0 = 10^{-14}\,\Omega$.m, $j_c = 10^{10}$ A.m^{-2} and using a rate of change of the magnetic field $\dot{B}(r,t) = 10^{-3}$ T.s^{-1} corresponding to the experimental conditions.

IV. RESULTS AND DISCUSSION

We will first discuss the results concerning the properties of the discontinuity lines emerging from the lithographically defined indentations. An analytical calculation of the functional form of the d-lines for different indentation shapes is deduced from the critical state model ($n \to \infty$). This is then used to fit the experimental data and afterwards compared with the case of finite n obtained by numerical modeling. The analysis of the excess flux Δ and the influence of indentation on the thermomagnetic instabilities is deferred to the sections thereafter.

A. Indentation induced discontinuity lines

1. *Functional form of the d-lines according to the critical state model*

In this section, we consider the critical state model for the penetration of the magnetic flux inside a superconductor in two different geometries: (i) *a longitudinal geometry*, e.g. a long cylinder or a slab subjected to a parallel magnetic field, and (ii) *a transverse geometry*, e.g. a thin film subjected to a perpendicular magnetic field.

The critical state model assumes that the superconducting regions which are subjected to a varying flux density, however small, develop 'maximal' shielding currents with a density j_c. The value of j_c results from an equilibrium between the vortex driving force $\mathbf{j} \times \mathbf{B}$ and the pinning force at the defects[25]. Upon an increase in the applied magnetic flux, the force balance is broken and vortices progress further into the superconductor until a new equilibrium is reached. The critical current density j_c depends in principle on the local value of the magnetic flux density B. In the following, we assume the simplest model with a constant j_c.

In the longitudinal geometry, an increase of the external magnetic flux induces shielding currents in the peripheral region of the superconductor and leaves the inner region flux-free. The resulting magnetic field decreases from the external boundary according to Ampere's law $\nabla \times \mathbf{H} = \mathbf{j}$, where $|\mathbf{j}| = j_c$ in the flux penetrated region, whereas both $\mathbf{H}$ and $\mathbf{j}$ vanish in the flux-free region.

In the transverse geometry, the magnetic flux and shielding current distributions are affected by demagnetizing effects. Moreover, even very small variations of the external magnetic field lead to shielding currents flowing over the entire film[26]. As a result, the sheet current density $\mathbf{J} = \int dz\, \mathbf{j}$ varies continuously over the area of the superconducting film, from $|\mathbf{J}| = J = 0$ to $J = j_c d$. Two distinct regions can then be identified: (i) a fully penetrated region with $J = j_c d$ and (ii) an inner flux-free region with $J < j_c d$ and $H_z = 0$. In the fully penetrated region, we have $|\nabla \times (g\hat{z})| = j_c d$, where g is the current stream function.

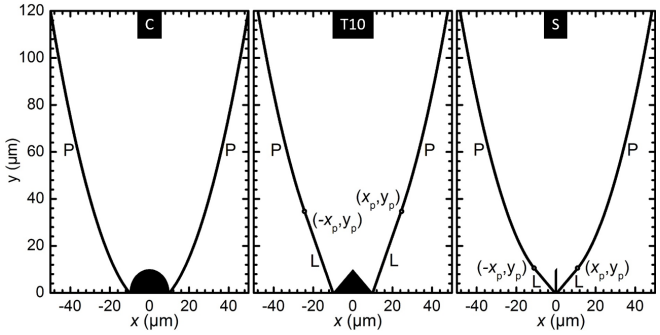

FIG. 4: Discontinuity-lines in the critical state model for defects of size $R = 10\,\mu$m: a semicircular indentation (C, left panel), a triangular indentation with $b = 20\,\mu$m (T10, middle panel) and a rectangular indentation with $b = 1\,\mu$m (S, right panel). The d-lines are described by parabola branches P, but for the T10 and S indentations, the branches in the vicinity of the defect ($y < y_P$) correspond to straight lines L.

We now turn to determine the equations of the d-lines emerging from an indentation within the critical state model, concentrating for each geometry on the fully penetrated regions. In both the longitudinal geometry (where $|\nabla \times \mathbf{H}| = j_c$) and the transverse geometry (where $|\nabla \times (g\hat{z})| = j_c d$), the magnetic flux penetration is characterized by a spatial decrease of H_z or g from the external boundary inwards with a constant gradient. As a result, the contour lines of H_z in the longitudinal geometry (or those of g in the transverse geometry) are at a constant perpendicular distance from the edges. Currents flow parallel to these contour lines and, in regions where two or more flux fronts meet, they undergo sharp changes of direction. These changes give rise to discontinuity lines, or d-lines, which appear at the locus of points equidistant from the edges of the sample, *including the edges of the indentation.*

Semicircular indentation.- For a semicircular indentation of radius R, the d-lines are defined as the locus of points equidistant from the straight edge and the arc of circle of radius R. This gives two arcs of parabola placed symmetrically about the indentation, described by[27]

$$y(x) = \frac{x^2}{2R} - \frac{R}{2}, \tag{12}$$

and illustrated in the left panel of Fig. 4

Triangular indentation.- A triangular indentation of width b and height R gives rise to two symmetric d-lines, each composed of two parts: (i) a straight line L, which is the locus of points equidistant from the straight edge and from one of the sides of the triangle, and (ii) a parabola branch P, corresponding to the locus of points equidistant from the straight edge of the sample and the tip of the triangle. For the right branch ($x > b/2$), we have

$$L: \quad y = (x - \frac{b}{2})\,\frac{b}{2R}\left(1 + \sqrt{1 + 4\,\frac{R^2}{b^2}}\right), \qquad (13)$$

$$P: \quad y = \frac{x^2}{2R} + \frac{R}{2}. \qquad (14)$$

These two curves join continuously (their derivatives are also continuous) at the point of coordinates

$$x_{\rm P} = \frac{b}{2}\left(1 + \sqrt{1 + 4\,\frac{R^2}{b^2}}\right), \qquad (15)$$

$$y_{\rm P} = \frac{b^2}{4R}\left(1 + \sqrt{1 + 4\,\frac{R^2}{b^2}}\right) + R. \qquad (16)$$

The left branch is obtained from a mirror symmetry operation $x \mapsto -x$, as illustrated in the middle panel of Fig. 4.

Rectangular indentation.- A rectangular indentation of width b and height R gives rise to two d-lines, each made of a straight line L, corresponding to points equidistant from the straight edge and from one of the indentation sides, and a branch of parabola P, corresponding to an equidistance from the straight edge and one the rectangle corners at $y = R$. The right branch ($x > b/2$) is given as

$$L: \quad y = x - \frac{b}{2}, \qquad (17)$$

$$P: \quad y = \frac{(x - b/2)^2}{2R} + \frac{R}{2}. \qquad (18)$$

The two curves join continuously (their derivatives are also continuous) at the point of coordinates

$$x_{\rm P} = \frac{b}{2} + R, \qquad (19)$$

$$y_{\rm P} = R. \qquad (20)$$

The left branch is obtained from a mirror symmetry operation $x \mapsto -x$, as illustrated in the right panel of Fig. 4.

It is noteworthy that independently of the shape of the indentation, the $d-$lines take the following asymptotic form for $y \gg R$:

$$y \approx \frac{x^2}{2R}, \qquad (21)$$

where R is the height of the defect.

2. *Experimental results*

In Fig. 5(a) we show a typical field pattern in a sample with a single indentation (T10), where the following characteristic parameters are indicated: the distance D between the flux front and the sample border, and the excess flux penetration Δ. The parabolic d-line determined by the local minima in the flux profile is highlighted by the white dashed line. The inhomogeneous penetration of the magnetic flux leads to an irregular flux front. This may be caused by uncontrolled edge defects of size comparable to $\xi(T) \approx 15$ nm or local changes in the material properties.

The spatial identification of the d-lines has been done numerically by searching in the plane of the sample the (x, y) coordinates where the intensity is minimum. The position of the sample border is defined by the line $y = 0$ and the indentation is centered at $x = 0$. An example of line profile of the magnetic field along the dotted straight line (black) depicted in the upper panel of Fig. 5(a) is shown in the lower panel of the same figure. Since the position of the d-lines is field independent, we present the data corresponding to the highest possible field exhibiting optimum contrast. The fitting is based on eq. (12), (14) and (18) and was limited to a distance $y = 100\,\mu$m from the border.

In Fig. 5(b), the d-lines for two different triangular indentations, T0.5 and T8, are plotted at the reduced temperature $T/T_{\rm c} = 0.68$. Within the Bean critical state model the d-lines follow a parabolic dependence as long as the indentation has a semicircular shape. As we pointed out above, for other shapes, the parabolic dependence remains applicable only for values of the y coordinate larger than $y_{\rm P}$. Since the largest size of the studied defects is 10 μm, while d-lines extend about 100 μm inside the sample, we can safely fit the experimentally determined discontinuity lines with $y = ax^2 + c$. We are particularly interested in the determination of the concavity a which, according to the critical state models, should be inversely proportional to the size R of the defect. In other words, a larger indentation should lead to a wider parabola. This trend is confirmed by the representative d-lines shown in Fig. 5(b).

In Fig. 5(c), the influence of size is studied for five triangular defects with sizes R between 0.5 μm and 10 μm. Even though the T10 indentation has a different aspect ratio than the other triangular defects, eq. (14) shows that the parabolic dependence is solely determined by the height of the triangle. The prediction of the Bean model for longitudinal geometry, $(2a)^{-1} = R$, is also plotted as a dashed line in the same figure. A clear discrepancy between the experimental data and the Bean model can be observed. First, the linear dependence between $(2a)^{-1}$ and R extrapolates to a finite a even if the defect is absent ($R = 0$)[28], as evidenced by the plain line used as a guide to the eye. Secondly, the R values deduced from the Bean model largely overestimate the actual size of the defects. These observations lead us to question the validity of Eq. (12) in the present study. In our case, an empirically estimated shift of 9 μm needs to be subtracted from the experimentally determined value of $1/2a$ in order to find the actual size of the defect. Possible sources of disagreement come from the fact that the Bean model for longitudinal geometry (i) neglects the surface barrier for vortex penetration, (ii) corresponds to an unrealistically

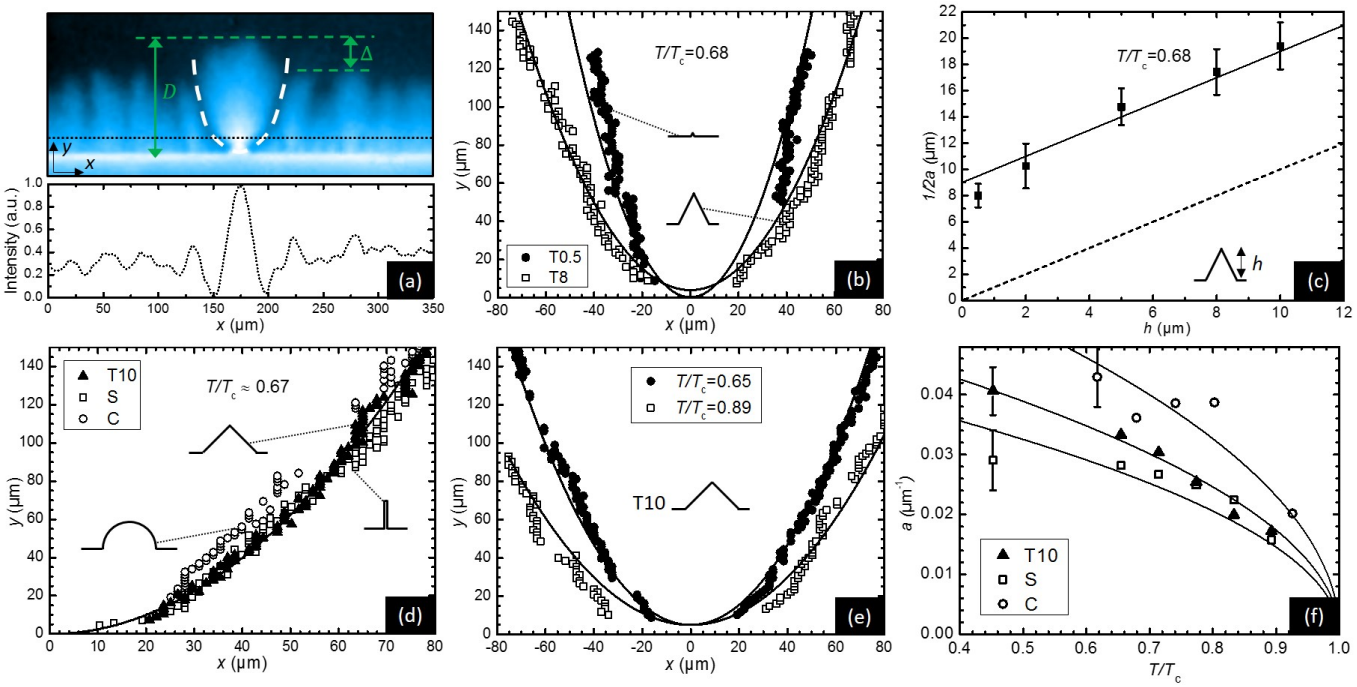

FIG. 5: (a) Field penetration for the T10 indentation at $T/T_c = 0.5$ (upper panel). The intensity profile shown in the lower panel is taken along the black dotted straight line and shows where the deep minima corresponding to the d-lines are located. We fit these d-lines with a parabola (white dashed line) of concavity a. The flux front penetration D and the excess flux penetration Δ measured from the sample border are also represented. In (b), parabolas are shown for the T0.5 and T8 indentations centered at $x = 0$. The sample border is at $y = 0$. As also represented in (c), an increase in the triangular indentation size leads to the widening of the parabolas. The solid line is used as a guide to the eye, while the dashed line shows the predictions of the Bean model for the longitudinal geometry. (d) For defects of the same size but with different shapes (C, S and T), there is little change in a. The raise of the temperature leads to a widening of the parabola, shown in (e) for the T10 indentation. The temperature dependence of a is shown in (f) for T10, S and C, where solid lines are used as guides to the eye. The error bar indicated for the first point of each indentation is valid for all the points belonging to the same group.

high creep exponent n, (iii) fails to describe the non-local nature of thin films, and (iv) assumes a field independent critical current density j_c.

Let us first discuss the influence of finite penetration field for vortex entry in samples with border defects.[10,29] Recent reports have shown that crowding of Meissner currents can severely affect the conditions for vortex entry in sharp-bends[10,30–33]. Within this scenario, border indentations of different shapes lead to different suppressions of the flux entry barrier. In particular, it was shown that triangular indentations should allow a more premature vortex entry than rounded indentations. Therefore, if current crowding (ignored in the Bean model) were an important ingredient to consider, we should be able to see its influence by changing the shape of the indentations. A comparison of d-lines obtained for three different shapes of indentation is presented in Fig. 5(d) at $T/T_c = 0.68$. Note that the curvature of the d-line emerging from the semicircular indentation is slightly bigger than for the triangular and slit indentations. Moreover, far away from the border defect, the curvature is smaller for the slit than for the triangular indentation. As it was demonstrated in the previous section, the d-lines emanating from a slit, a triangular or a semicircular defect, do not follow exactly the same functional form. For a given y_0 coordinate, the local Bean model predicts that the x_0 loci of the d-line should be the largest for the circular defect and smallest for the triangular, in contrast to what is observed experimentally. Although these results seem to indicate that current crowding may indeed play a role, the observed minor differences suggest that its effect in the form of the parabolic d-line is rather small. In the next section, we will see that current crowding effects manifest themselves in a substantial increase of the excess penetration distance Δ.

Assessing the relevance of the creep exponent n on the flux entrance can be experimentally done by changing temperature. Indeed, since $n = U_0/k_B T$, where U_0 is the activation energy over the pinning barrier, n decreases as the temperature increases, reaching the Ohmic value $n = 1$ at the vortex liquid phase very close to T_c.[34] In Fig. 5(e), the temperature dependence of the flux penetration is plotted at two different temperatures for the triangular indentation T10. The increase of the temperature leads to a significant opening of the parabola, i.e. a decrease of the concavity a. In Fig. 5(f), the temperature dependence of the concavity is shown for the T10, S and C indentations. Remarkably, the progressive open-

ing of the parabolic d-lines as temperature increases is at odds with the theoretical predictions of Ref. 8 which foresees a discontinuity line rather independent of the n value. A possible explanation for this effect is the fact that the first vortex penetration field $H_{\rm p}$ is lowered at the indentation compared to its value elsewhere. Since current crowding is more severe as n approaches unity, when T approaches $T_{\rm c}$, the difference between $H_{\rm p}$ at the border and at the indentation will increase, causing the entering flux to spread around the indentation.

The influence of the border's roughness on the parabolic d-lines has also been studied by comparing samples with smooth (P) and rough (R) borders. While the penetration dynamics is different, with flux entering the sample smoothly in the R borders and in small jumps in the P borders, the d-lines are not affected by the roughness of the edges for mean values of roughness ten times smaller than the indentation size. In order to artificially create a roughness similar to the indentation size, we designed samples with borders featuring several indentations of the same size, arranged in a periodic pattern (T10p0, T10p10, T10p50 and T10p100 borders). In these samples, we found no difference between the parabolic d-lines originating from the indentations and the d-lines for a single T10 indentation, as long as the distance between the indentations is big compared to y. When y becomes comparable to the distance between indentations, the d-lines interfere and follow a line perpendicular to the sample border, exactly in the middle of two neighbouring indentations. Such configuration of d-lines was already suggested for the magnetic flux penetration in bulk superconductors with a periodic array of holes[35].

3. Numerical results

Unfortunately, it is difficult to determine experimentally the influence of demagnetization effects on the curvature a of the d-lines. This would imply the investigation of a large range of sample thicknesses, assuming that the superconducting properties themselves are not influenced by this change. Instead, in this section, we perform a theoretical modelling of the system allowing us to compare the longitudinal and transversal geometries, as well as the impact of the creep exponent and the field dependence of the critical current density.

The dependence of $1/2a$ on the creep exponent n, obtained from the numerical modelling of the T10 sample, is summarized in Fig. 6 for the case of a full magnetic field penetration, as in the experiments. The corresponding parabolic d-lines are extracted using the same algorithm as for the experimental data, which gives results similar to the streamlines of h as shown in Fig. 3. The dashed line corresponds to what is predicted by the Bean model ($j_{\rm c}$ constant) in the longitudinal geometry. Simulations for the longitudinal geometry, in the case of finite values of the creep exponent n and constant $j_{\rm c}$, are shown with

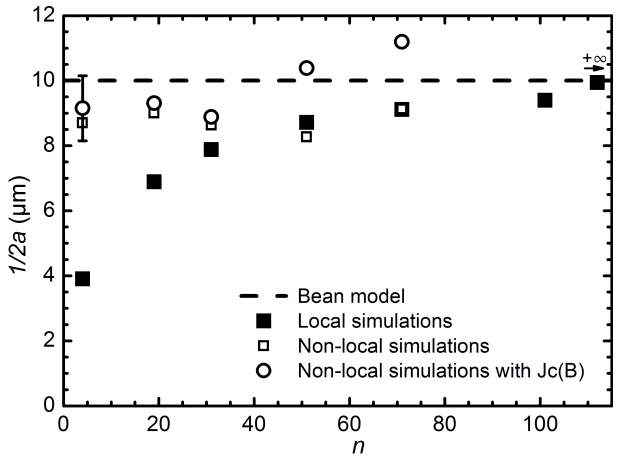

FIG. 6: Numerical simulations of $1/2a$ for the T10 indentation, where a is the concavity of the parabola fitting the d-lines. The dashed line shows the value obtained for the critical state model. The parabolas in the local case (full squares) yield values of $1/2a$ smaller than for the Bean model, while the Bean model limit is recovered for $n \to \infty$. The non-local case and its extension to account for the field dependence of the current, based on the experimental data of Fig. 2(b), slightly modify $1/2a$, but remain below the Bean model limit.

solid squares. Note that $1/2a$ is smaller for finite n than for $n \to \infty$ (Bean model). In other words, the more realistic model of finite creep exponent predicts parabolic d-lines with curvature larger than in the Bean model. The fact that the concavity increases as n decreases is at odds with the experimental results. Indeed, since $n \propto T^{-1}$, we observe experimentally that $1/2a$ increases as n decreases.

Introducing demagnetizing fields (non-local case) also modifies the concavity of the d-lines. This is shown by the open square symbols in Fig. 6. In particular, demagnetizing effects lead to a broadening of the parabola when compared to the longitudinal geometry, although the values of $1/2a$ still remain below the dashed line obtained from the Bean model. In order to account for the field dependent $j_{\rm c}(B)$ shown in the inset of Fig. 2(b), we have modified Eq. (2) by using $j_{\rm c}(B) = j_0(B_{\rm c2}/B)^{\gamma}$,[36] with γ and $B_{\rm c2}$ obtained from fitting the experimental data. The results are represented by the open circles in Fig. 6 and lead to a further opening of the parabola. This result is in agreement with what has been suggested in Ref. 7,37. In the limit $n \to \infty$, we expect the field dependent non-local case to converge towards the results of the local case, $1/2a = 10\,\mu$m. The fact that there is no significant deviation with respect to the situation with no field dependence at all is consistent with the results of Ref. 36, where the authors showed that increasing the exponent γ is equivalent to increasing the effective creep exponent.

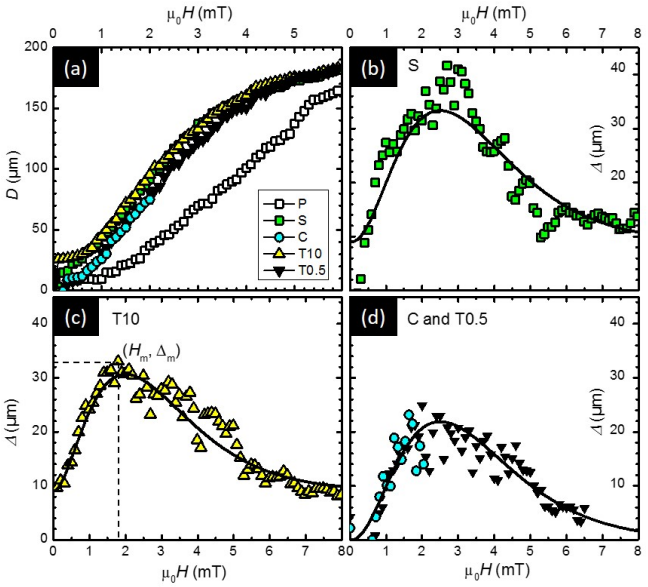

FIG. 7: Panel (a) shows the distance D between the flux front penetration at the indentation and the border at $T/T_c = 0.5$ for the T10, T0.5, S and C indentations and for a plain film (P) without indentations. Flux penetration is enhanced at the indentations compared to the plain film. This effect is shown in panels (b)-(d), where the difference Δ between the flux front at the indentation and at the smooth border surpasses several times the actual size of the indentation. The lines are guides to the eye.

B. Excess flux penetration

The border indentation produces an enhancement of the magnetic flux penetration when compared to the penetration along the smooth border. This excess flux penetration has been quantified by Vestgården *et al.*[4] by introducing a parameter Δ corresponding to the distance between the flux fronts originating from the indentation and those developing from the smooth border (see Fig.5(a)). Based on numerical simulations, these authors predict that Δ should be field independent and equal to the size of the defect (R) in the case of the Bean model in the longitudinal configuration (i.e. without demagnetization effects), whereas a non-monotonous function $\Delta(H)$, with a maximum value exceeding the defect size at $H = H_m$ and decreasing as H further increases, should be obtained for thin films in the transversal geometry, dominated by non-local effects. As suggested by these authors, the ultimate reason for the excess penetration distance is that Meissner currents concentrate in front of the indentation (current crowding), where their density reaches j_c, and hence lead to even deeper flux penetration. This is why the flux front near the indentation advances faster than in the rest of the film for $H < H_m$.

In order to corroborate these predictions, we measured $\Delta(H)$ experimentally by performing zero field cooling experiments on the samples presented in Fig. 1. The temperature was set at $T/T_c = 0.5$. The magnetic field $\mu_0 H$ was then gradually increased by steps of 0.01 mT and images were recorded for each step. We defined the magnetic flux front as the iso-field line corresponding to a threshold value of the magnetic field. This translates to a threshold intensity I_{thres}, calculated in each image with the following formula:

$$I_{thres} = I_{center} + \frac{1}{2}(I_{out} - I_{center}), \qquad (22)$$

where I_{center} is the intensity at the sample center ($B \sim 0$) and I_{out} is the intensity far away from the sample ($B \sim H$) . These values are calculated by averaging the intensity in 5×5 px^2 squares.

Fig. 7(a) shows the evolution of the distance D between the sample border and the flux front emerging from the indentation (see Fig. 5(a)) as H increases. The distance D for the plain film (P) rises monotonically as the field increases and tends towards 200 μm, the half-width of the sample, when the flux has invaded the whole sample. For the samples featuring an indentation, the high field limit remains the same since it corresponds to a geometrical constraint, but the values of D for intermediate H are significantly higher. This behavior evidences the fact that the flux penetration is enhanced at the indentations. We notice that D is slightly smaller for indentations C and T0.5 than for S and T10, likely due to less severe current crowding effects for smaller and round-shaped defects.

In order to determine Δ, we compute the difference between D at the position of the indentation and away from the indentation, where the flux penetration is undisturbed.[38] Fig. 7(b)-(d) shows the obtained $\Delta(H)$ for C, S, T10 and T0.5 defects. The data points concerning samples T0.5 and C have been truncated because magnetic domains coming from the garnet suddenly appeared in the images, thus perturbing the flux distribution in the superconductor. The general shape is the same for all curves: for low H, Δ increases as the field increases and reaches a maximum value Δ_m, larger than the defect size R, at fields $\mu_0 H_m$ between 2 and 3 mT. In other words, for $H < H_m$, the flux penetrates into the sample more easily via the indentation than through the smooth border. For $H > H_m$, the tendency inverts since the progression of the flux front emerging from the indentation slows down when approaching the center of the sample, as illustrated in Fig. 7(a). It it important to point out that the noisy appearance of the curves does not correspond to limitations in the measurement technique, but are inherent to the physical process under study. Indeed, the flux propagates into the sample in a discontinuous way, progressing by small jumps of several micrometers, which are reflected in the $\Delta(H)$ curves, as clear oscillations.

It was shown in Ref. 4 that a larger defect gives rise to a larger Δ_m. This is confirmed in our experiments when comparing the samples T10 and T0.5. We find experimentally that Δ_m can be several times larger than the defect size, whereas an increase of about 50% was re-

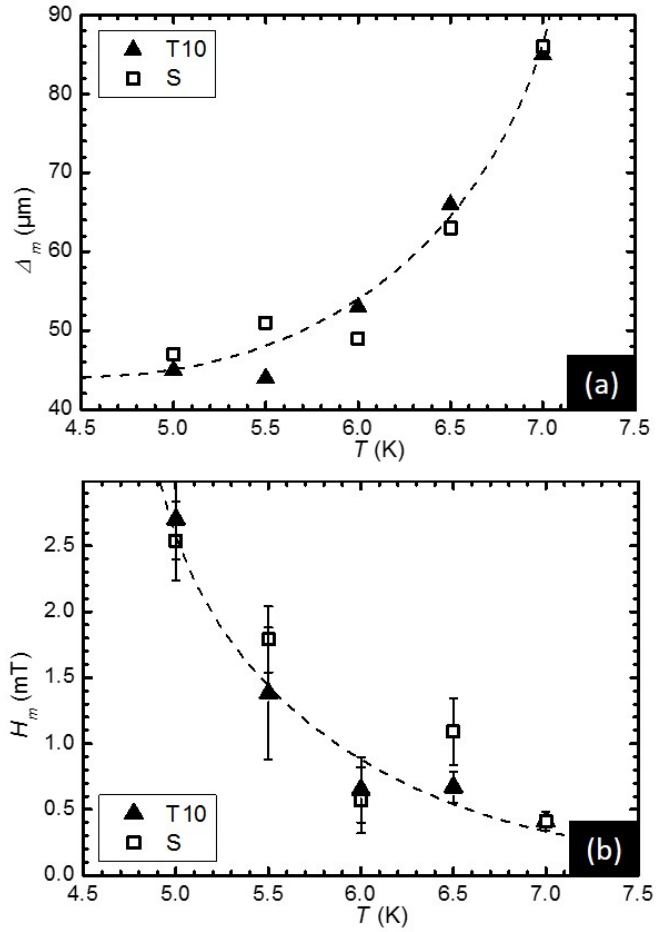

FIG. 8: Temperature dependence of the maximum excess flux penetration Δ_m (a) and its corresponding field H_m (b). The dotted lines are guides to the eye.

ported theoretically[4]. Note that current crowding effects could account for the fact that Δ_m is larger for the S and T10 defects than for the C defect. All in all, our measurements in clean and well defined border indentations seem to confirm the general trend of the magnetic flux front evolution predicted by Vestgården *et al.*[4].

As we pointed out in the introduction, Ref. 4 also predicts that as n increases, both Δ_m and H_m increase. Since n decreases by increasing T, we expect a decrease of Δ_m and H_m with increasing temperature. Fig. 8 shows the temperature dependence of Δ_m and its corresponding field H_m is shown in panel (b) of the same figure. Although H_m is a decreasing function of T, as predicted numerically, $\Delta_m(T)$ shows a tendency opposed to the predictions. This discrepancy between theory and experiment can be explained by a more rapid decrease of j_c when increasing temperature, as compared to the difference $H_2 - H_1$ between the first penetration fields at the indentation and at the smooth border. Vodolazov *et al.*[39] have investigated theoretically the influence of sample defects in the penetration of vortices in a homogeneous superconductor. These authors concluded that the presence of surface defects causes a drop in the first penetration field and leads to a qualitative change in the magnetization curve. Unfortunately, there is no detailed investigation of the temperature dependence of this effect, but we can safely assume that, as for the smooth border, the penetration field at the defect also decreases when the temperature raises. Therefore, also $H_2 - H_1$ should decrease with increasing T. In a first approximation (Bean critical state model), the difference Δ between the flux front positions goes as $\Delta \sim (H_2 - H_1)/j_c$. If the inevitable decrease of j_c when T raises is faster than the decrease of $H_2 - H_1$, we speculate that Δ should increase with T, as observed in the experiments. Clearly, further numerical studies will be necessary to unambiguously pinpoint the origin of the reported effect.

C. Flux avalanches in indented samples

Due to the large electric fields and the larger traffic of vortices at defects, it is widely believed and repeatedly predicted that indentations should represent preferred nucleation spots for the development of thermomagnetic instabilities.[2–4] In order to corroborate this hypothesis we performed both field cooling and zero-field cooling experiments to observe the position of avalanches in the Nb film with a periodic row of indentations (T10p100 and T10p50) as well as in the T10 and S samples.

In Fig. 9(a), we show the flux penetration in a sample with optimum borders after zero-field cooling at 3.6 K and applied field $\mu_0 H = 2$ mT. In this sample, the top defect is S and the bottom corresponds to T10. No evidence of flux avalanches is observed. However, by applying a magnetic field of 12.5 mT before cooling down to 3.6 K, and subsequently reducing the field to 1 mT, clear avalanches of negative flux (i.e. polarity opposed to the applied field) are observed as shown in Fig. 9(b). Note that the thermomagnetic instabilities are not triggered at the indentations, in striking contrast to what was expected.

Panels (c) and (d) of the same figure show a geometry similar to panels (a) and (b), but now the indentations are positioned along rough (R) borders (Fig. 1), while the short indentation-free borders are smooth. In this case, for both zero-field-cooling (Fig. 9(c)) and field-cooling (Fig. 9(d)), avalanches are triggered at the smooth short side of the sample, not in the vicinity of the indentations. This confirms the fact that smooth borders are more prone to exhibit avalanches than rough borders. Adding more indentations, as shown in Fig. 9(e) and (f), does not help to force the instabilities to be triggered at this electric field hot spots.

A possible explanation for this surprising result might involve an effective reduction of the critical current density at the indentation as a consequence of the reduction of the surface barrier for vortex entrance, as discussed in Ref. 10. In simple words, the indentation seems to act as a magnetic flux faucet that helps to release the magnetic

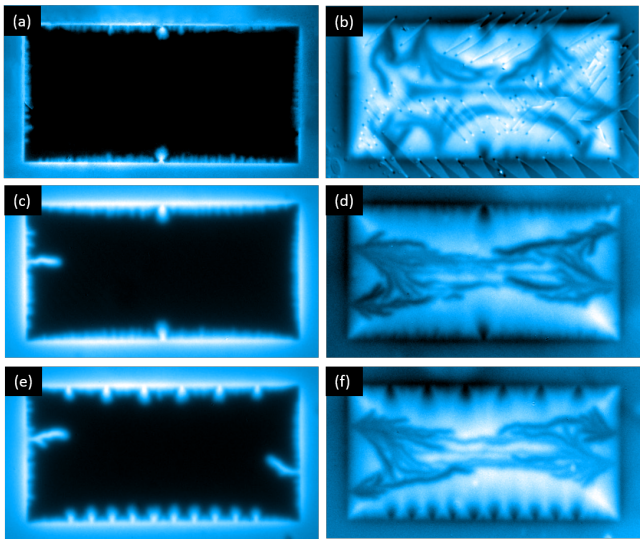

FIG. 9: MO images of the Nb film at 3.6 K show the flux penetration (a,c,e) when a 2 mT magnetic field is applied after ZFC or (b,d,f) in a 1 mT field after FC in 12.5 mT. In (a-d), the samples feature the S (top) and T10 (bottom) indentations, while (e) and (f) show the T10p100 (top) and T10p50 (bottom) indentations. Contrarily to what was predicted in the literature, avalanches are not preferentially triggered at indentations, as they decrease the magnetic pressure, but tend to appear at the smooth borders. The comparison of samples (a,b,e,f), having four smooth sides, with (c,d), having rough long-sides (R) shows the importance of smooth borders to trigger avalanches.

pressure at the sample border by enhancing the smooth flux penetration in its vicinity.

V. CONCLUSION

The present investigation reveals unexpected features of discontinuity lines generated by border defects in Nb thin film superconductors. In particular, we find out that (i) the concavity of the parabolic d-lines is smaller than what is expected from the Bean model for longitudinal geometry, and (ii) against the common wisdom, indentations are not inducers of thermomagnetic instabilities that cause flux avalanches. We demonstrate that the d-lines encode information about the demagnetization effects, the size and shape of the defect, the creep exponent n, and the field dependence of the critical current density. However, none of these ingredients is able to fully account for the observed effects. We speculate that a premature flux penetration at the indentation due to a reduction of the threshold field for the first vortex penetration, not included in the macroscopic description of the electrodynamics of superconducting films, could be the cause of the puzzling results. Further investigations on samples with artificial defects placed away from the border, and thus not influencing the surface barrier, may provide a way to discern the influence of first vortex nucleation on the d-lines.

It has been shown that macroscopic drilled holes in high-T_c superconductors, introduced with the aim to improve oxygen diffusion and heat exchange, need to be placed strategically along the d-lines generated by neighbouring holes if trapped magnetic flux is to be maximized.[35] A similar study in thin films, where d-lines are influenced by non-local effects, may be of technological interest.

Acknowledgments

This work was partially supported by the Fonds de la Recherche Scientifique - FNRS, the ARC grant 13/18-08 for Concerted Research Actions, financed by the French Community of Belgium (Wallonia-Brussels Federation), the Brazilian National Council for Scientific and Technological Development (CNPq) and the São Paulo Research Foundation (FAPESP), Grant No.2007/08072-0, and the program for scientific cooperation F.R.S.-FNRS-CNPq V 4/225 - NR/DeM - 2.327. J. B. acknowledges support from F.R.S.-FNRS (Research Fellowship). The work of A. V. S. is partially supported by "Mandat d'Impulsion Scientifique" MIS F.4527.13 of the F.R.S.-FNRS.

[1] E. H. Brandt, Phys. Rev. B **52**, 15442 (1995).
[2] Th. Schuster, H. Kuhn, and E. H. Brandt, Phys. Rev. B **54**, 3514 (1996).
[3] Th. Schuster, M. V. Indenbom, M. R. Koblischka, H. Kuhn, and H. Kronmüller , Phys. Rev. B **49**, 3443 (1994).
[4] J. I. Vestgården, D. V. Shantsev, Y. M. Galperin, and T. H. Johansen, Phys. Rev. B **76**, 174509 (2007).
[5] M. Campbell, and J. E. Evetts, Critical Currents in Superconductors, Taylor and Francis, London (1972).
[6] Ch. Jooss, J. Albrecht, H. Kuhn, S. Leonhardt, and H. Kronmüller, Rep. Prog. Phys. **65**, 651 (2002).
[7] Ch. Jooss, R. Warthmann, A. Forkl, and H. Kronmüller, Physica C **299**, 215 (1998).
[8] A. Gurevich, and M. Friesen, Phys. Rev. B **62**, 4004 (2000).
[9] M. Friesen, and A. Gurevich, Phys. Rev. B **63**, 064521 (2001).
[10] D. Cerbu, V. N. Gladilin, J. Cuppens, J. Fritzsche, J. Tempere, J. T. Devreese, V. V. Moshchalkov, A. V. Silhanek, and J. Van de Vondel, New J. Phys. **15**, 63022 (2013).
[11] J. R. Clem, and K. K. Berggren, Phys. Rev. B **84**, 174510 (2011).
[12] M. Motta, F. Colauto, J. I. Vestgården, J. Fritzsche, M. Timmermans, J. Cuppens, C. Attanasio, C. Cirillo, V. V. Moshchalkov, J. Van de Vondel, T. H. Johansen, W. A. Ortiz, and A. V. Silhanek, Phys. Rev. B **89**, 134508 (2014).
[13] Z. Jing, H. Yong, and Y.-H. Zhou, Supercond. Sci. Technol.

28, 75012 (2015).

[14] A spectral analysis of the roughness shows no clear periodicity, confirming an inherent randomness. This is also consistent with the fabrication method. Indeed, the difference between the smooth and the rough samples is the x and y electron beam step size of the scanning electron microscope when patterning the samples. The smooth samples were patterned with the highest resolution, 1 pixel × 1 pixel, corresponding to steps of 12.5×12.5 nm^2. The rough samples were written with a 4 pixels × 4 pixels resolution which is 50×50 nm^2. The area dose was the same in both cases. Thus for the rough sample, the SEM stays in the middle of a 50×50 nm^2 area 16 times longer than on a 12.5×12.5 nm^2 area. A slight randomness of the middle position within these 50×50 nm^2 areas is the origin for the artificial roughness we obtained. This effect is further magnified during subsequent steps of the fabrication process (Al deposition and etching).

[15] M. R. Koblischka, and R. J. Wijngaarden, Supercond. Sci. Technol. **8**, 199 (1995).

[16] P. E. Goa, H. Hauglin, Å. A. F. Olsen, M. Baziljevich, and T. H. Johansen, Rev. Sci. Instrum. **74**, 141 (2003).

[17] M. Tokunaga, T. Tamegai, and T. H. Johansen, Physica C **437-438**, 331 (2006).

[18] M. Motta, F. Colauto, W. A. Ortiz, J. Fritzsche, J. Cuppens, W. Gillijns, V. V. Moshchalkov, T. H. Johansen, A. Sanchez, and A. V. Silhanek, Appl. Phys. Lett. **102**, 212601 (2013).

[19] J. I. Vestgården, D. V. Shantsev, Y. M. Galperin, and T. H. Johansen, Phys. Rev. B **77**, 014521 (2008).

[20] J. I. Vestgården, V. V. Yurchenko, R. Wördenweber, and T. H. Johansen, Phys. Rev. B **85**, 014516 (2012).

[21] J. I. Vestgarden, D. V. Shantsev, A. A. F. Olsen, Y. M. Galperin, V. V. Yurchenko, P. E. Goa, and T. H. Johansen, Phys. Rev. Lett. **98**, 117002 (2007).

[22] COMSOL Multiphysics software with the Coefficient Form PDE.

[23] E. H. Brandt, Phys. Rev. B **72**, 024529 (2005).

[24] J. I. Vestgården, P. Mikheenko, Y. M. Galperin, and T. H. Johansen, New J. Phys **15** 93001 (2013).

[25] A. M. Campbell, and J. E. Evetts, Adv. Phys. **21**, 199 (1972).

[26] E. H. Brandt, Phys. Rev. Lett. **74** 3025 (1995).

[27] A. Forkl, and H. Kronmüller, Phys. Rev. B **52** 16130 (1995).

[28] This seemingly non-causal result for the simple extrapolation to R = 0 indicates that the inverse concavity of the parabola must increase abruptly from zero within a very narrow interval of the indentation size.

[29] J. Gutierrez, B. Raes, J. Van de Vondel, A. V. Silhanek, R. B. G. Kramer, G. W. Ataklti, and V. V. Moshchalkov, Phys. Rev. B **88**, 184504 (2013).

[30] H. L. Hortensius, E. F. C. Driessen, T. M. Klapwijk, K. K. Berggren, and J. R. Clem, Appl. Phys. Lett. **100**, 182602 (2012).

[31] D. Henrich, P. Reichensperger, M. Hofherr, J. M. Meckbach, K. Il'in, M. Siegel, A. Semenov, A. Zotova, and D. Yu. Vodolazov, Phys. Rev. B **86**, 144504 (2012).

[32] J. R. Clem, Y. Mawatari, G. R. Berdiyorov, and F. M. Peeters, Phys. Rev. B **85**, 144511 (2012).

[33] O.-A. Adami *et al.*, Appl. Phys. Lett. **102**, 052603 (2013).

[34] M. F. Schmidt, N. E. Israeloff, and A. M. Goldman, Phys. Rev. Lett. **70**, 2162 (1993).

[35] G. P. Lousberg, M. Ausloos, Ph. Vanderbemden, and B. Vanderheyden, Supercond. Sci. Technol. **21**, 25010 (2008).

[36] D. V. Shantsev, Y. M. Galperin, and T. H. Johansen, Phys. Rev. B **65**, 184512 (2002).

[37] Ph. Vanderbemden, Z. Hong, T. A. Coombs, S. Denis, M. Ausloos, J. Schwartz, I. B. Rutel, N. H. Babu, D. A. Cardwell, and A. M. Campbell, Phys. Rev. B **75** 174515 (2007).

[38] An alternative way of determining Δ consists in computing the difference between the maximum D for a sample with a border defect and D for the plain film without defects. This approach leads to similar results to those presented in the manuscript, although the reliability is lower considering that involves the comparison of two different samples.

[39] D. Y. Vodolazov, I. L. Maksimov, and E. H. Brandt, Physica C **384**, 211 (2003).